

Vibrational shape tracking of atomic force microscopy cantilevers for improved sensitivity and accuracy of nanomechanical measurements

This content has been downloaded from IOPscience. Please scroll down to see the full text.

2015 Nanotechnology 26 045701

(<http://iopscience.iop.org/0957-4484/26/4/045701>)

View [the table of contents for this issue](#), or go to the [journal homepage](#) for more

Download details:

IP Address: 132.163.81.20

This content was downloaded on 15/01/2015 at 17:51

Please note that [terms and conditions apply](#).

Vibrational shape tracking of atomic force microscopy cantilevers for improved sensitivity and accuracy of nanomechanical measurements

Ryan Wagner^{1,2}, Jason P Killgore³, Ryan C Tung³, Arvind Raman^{1,2} and Donna C Hurley³

¹ School of Mechanical Engineering, Purdue University, West Lafayette, IN 47907, USA

² Birck Nanotechnology Center, Purdue University, West Lafayette, IN 47907, USA

³ Material Measurement Laboratory, National Institute of Standards and Technology, Boulder, Colorado 80305⁴, USA

E-mail: donna.hurley@nist.gov

Received 14 July 2014, revised 27 October 2014

Accepted for publication 25 November 2014

Published 5 January 2015



CrossMark

Abstract

Contact resonance atomic force microscopy (CR-AFM) methods currently utilize the eigenvalues, or resonant frequencies, of an AFM cantilever in contact with a surface to quantify local mechanical properties. However, the cantilever eigenmodes, or vibrational shapes, also depend strongly on tip–sample contact stiffness. In this paper, we evaluate the potential of eigenmode measurements for improved accuracy and sensitivity of CR-AFM. We apply a recently developed, *in situ* laser scanning method to experimentally measure changes in cantilever eigenmodes as a function of tip–sample stiffness. Regions of maximum sensitivity for eigenvalues and eigenmodes are compared and found to occur at different values of contact stiffness. The results allow the development of practical guidelines for CR-AFM experiments, such as optimum laser spot positioning for different experimental conditions. These experiments provide insight into the complex system dynamics that can affect CR-AFM and lay a foundation for enhanced nanomechanical measurements with CR-AFM.

Keywords: atomic force microscopy, contact resonance AFM, nanomechanical properties

(Some figures may appear in colour only in the online journal)

1. Introduction

The ability to accurately measure material properties at nanometer length scales is a critical challenge in the design and manufacture of many emerging materials and systems. Given its nanoscale spatial resolution, methods based on atomic force microscopy (AFM) [1] are well suited to meet this need. Of particular importance are nanoscale mechanical properties including elasticity, plasticity, adhesion, friction, and wear, as they can significantly influence macroscale behavior. A variety

of AFM methods have been developed to measure nanomechanical properties. One widely used technique, force-displacement spectroscopy, operates in quasistatic contact [2]. However, other techniques have been developed to overcome the limitations of quasistatic operation by exploiting the vibrational dynamics of the AFM cantilever [3].

One such dynamic AFM method for measuring nanomechanical properties is contact resonance atomic force microscopy (CR-AFM), a class of AFM techniques that includes sample-excited atomic force acoustic microscopy (AFAM) [4] and base-excited ultrasonic AFM (U-AFM) [5]. In CR-AFM, the cantilever tip is placed in contact with the sample, and a resonant vibration of the cantilever is excited. A

⁴ Partial contribution of NIST, an agency of the US government; not subject to copyright in the US.

resonant frequency, or eigenvalue, of the surface-coupled cantilever is then tracked as the cantilever is scanned over the sample. CR-AFM exploits the sensitivity of the resonant frequency f and quality factor Q to tip-sample contact stiffness and damping [6]. Measurements of f and Q can be related to spring and dashpot boundary conditions in a dynamic Euler–Bernoulli beam model, and a contact mechanics model can then be utilized to determine the elastic and viscoelastic properties of the sample. CR-AFM has been used to measure the nanomechanical properties of a wide variety of material systems (see, e.g., [7–10]) and can be adapted to nanomechanical mapping [11–14].

In CR-AFM the eigenmodes, or the vibrational mode shapes, of the AFM cantilever are also sensitive to the tip-sample contact stiffness. Because contact stiffness depends directly on sample elastic modulus, the eigenmodes vary as the tip scans across different sample regions. This is in sharp contrast to more commonly studied intermittent contact (IC-AFM) methods, in which the cantilever eigenmodes are only slightly perturbed versions of the eigenmodes of a freely vibrating cantilever. For this reason, in IC-AFM equivalent point-mass models can be constructed for each eigenmode based on the equivalence of the kinetic, strain, and tip-sample interaction energies of the free eigenmodes [15]. However, such traditional AFM point mass models are inaccurate for CR-AFM. Accurate analysis requires use of a continuum beam model with complex boundary conditions to derive material properties from the observed f and Q [16].

Detailed knowledge of CR-AFM eigenmodes could potentially improve the method’s capabilities for quantitative nanomechanical measurements. To date, this knowledge has almost always been inferred from a mathematical model of cantilever dynamics [6, 17]. Previous experimental work [8, 18] was rather limited in scope and focused only on the practical goal of improving signal detection. Measurement of real eigenmode shapes could capture deviations from model behavior and thus improve analysis accuracy compared to using the idealized beam geometry employed in a theoretical model. Knowledge of cantilever eigenmodes also provides a potential alternate pathway for the determination of contact stiffness through energy-based calculations. Finally, deeper knowledge of the mode shapes encountered for the wide range of contact stiffnesses in typical CR-AFM experiments allows for better optimization of the experimental setup. These combined benefits make measurements and demonstration of the experimental stiffness sensitivity of cantilever vibration shapes particularly valuable.

Recently, a method was developed to measure the vibrating shape of an AFM cantilever in a commercial AFM instrument by rastering the laser used in the optical beam detection system [19]. This method can be implemented *in situ* in any commercial AFM instrument that provides motor-controlled laser spot positioning. Furthermore, this method does not require additional external equipment beyond that necessary for cantilever actuation, and in principle can be used to study the cantilever vibration in any dynamic AFM mode.

In this work, we have applied the laser raster optical beam method to study the dynamics of the AFM cantilever in CR-

AFM over a wide range of tip-sample stiffness. We control tip-sample stiffness with use of a suspended microbridge structure whose flexural stiffness varies continuously across its length. This allows for the direct measurement of the cantilever vibration shape (i.e., eigenmode) and resonant frequency (i.e., eigenvalue) as a function of tip-sample stiffness. The stiffness range encompasses that of typical CR-AFM measurements. Across this range of stiffness, we experimentally and theoretically compare the sensitivities of vibration shape and resonant frequency to stiffness. We also discuss how measurements of vibration shape can be used to optimize experimental setup and operating parameters. Our measurements provide new insight into the dynamics of the AFM cantilever, with both practical and theoretical implications for CR-AFM measurements.

2. Materials and methods

Experiments were performed on a commercial AFM instrument (Cypher S, Asylum Research/Oxford instruments)⁵. The detection laser wavelength was 860 nm, and the laser spot was approximately 30 μm long and 15 μm wide. Cantilever resonances were excited by a broadband, heavily damped piezoelectric transducer mounted beneath the sample (Contact Resonance Sample Actuator, Asylum Research). Two different cantilevers were used. Cantilever A (FMR, Nanosensors, Germany) had static bending stiffness $k_c = (2.69 \pm 0.16) \text{ N m}^{-1}$, nominal length $L_c = (225 \pm 10) \mu\text{m}$, and free flexural resonance frequencies of the n th eigenmode $f_{n,\text{free}} = (75.9 \pm 0.1, 475.8 \pm 0.1, 1332 \pm 1, 2604 \pm 1) \text{ kHz}$ for $n = (1, 2, 3, 4)$, respectively. Cantilever B (CONTR, Nanosensors, Germany) exhibited $k_c = (0.11 \pm 0.02) \text{ N m}^{-1}$, $L_c = (450 \pm 10) \mu\text{m}$, and $f_{n,\text{free}} = (12.6 \pm 0.1, 79.9 \pm 0.1, 224.3 \pm 0.1, 439.6 \pm 0.1) \text{ kHz}$ for $n = (1, 2, 3, 4)$, respectively. k_c is a property of an individual cantilever and is equal to the average force applied to the cantilever at the tip in the direction normal to the sample surface divided by the average displacement of the cantilever at the tip in the same direction. Values of k_c were determined with the corrected thermal method [20, 21]. Both cantilevers had reflective coatings to ensure that a near-constant laser intensity was delivered to the photodiode.

To study changes in cantilever vibration shape, it is useful to have an experimental sample that can provide a smooth variation in tip-sample stiffness. As shown in figure 1, one such sample is a suspended bridge structure. The static bending stiffness of the bridge $k_b(x_b)$ as a function of bridge position x_b should span a stiffness range comparable to that typical of CR-AFM experiments. A silicon (Si) ‘microbridge’ was fabricated with silicon-on-insulator microlithographic techniques. The scanning electron micrograph in figure 1(a) shows that the microbridge was approximately 800 nm wide, 250 nm thick, and 20 μm long. Assuming fixed–fixed boundary conditions, a rectangular cross section,

⁵ Certain commercial equipment, instruments, or materials (or suppliers, or software, etc) are identified in this paper to foster understanding. Such identification does not imply recommendation or endorsement by the National Institute of Standards and Technology, nor does it imply that the materials or equipment identified are necessarily the best available for the purpose.

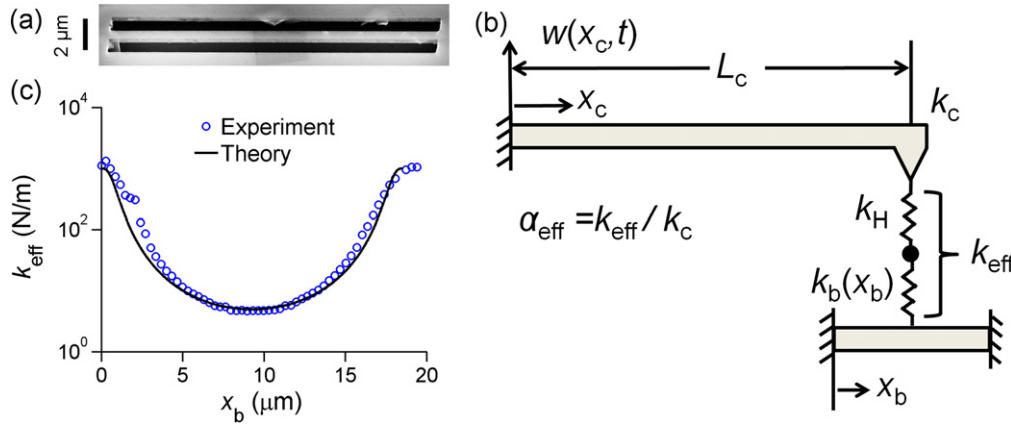


Figure 1. (a) Scanning electron microscopy image of microbridge sample. (b) Model of the cantilever-microbridge system. The effective contact stiffness $k_{\text{eff}}(x_b)$ experienced by the cantilever tip is a series combination of the bridge spring $k_b(x_b)$ and the spring associated with Hertzian contact mechanics model k_H , i.e., $1/k_{\text{eff}}(x_b) = 1/k_b(x_b) + 1/k_H$. The normalized effective contact stiffness is given as $\alpha_{\text{eff}} = k_{\text{eff}}/k_c$, where k_c is the static bending stiffness of the AFM cantilever. The applied experimental method will be concerned with measuring the transverse cantilever motion w as a function of position x_c along the length L_c of the cantilever and of time t . (c) k_{eff} versus bridge position x_b . Effective stiffness was measured with both static force–distance curves and CR-AFM experiments (blue data points) and calculated with Euler–Bernoulli beam theory (black curve). The black curve has been matched to the experimental data by choosing a value of k_H such that theory and experiment match at the clamped edges of the bridge and choosing a value of $E_b I_b / L_b^3$ for the bridge such that theory and experiment match at the center of the bridge.

and modulus and density for Si of 160 GPa and 2650 kg m^{-3} , respectively, the frequency of the first flexural resonance of the microbridge is approximately 5.32 MHz. As long as the surface-coupled cantilever is excited at frequencies below this resonant frequency, the bridge acts as a spring without any inertia. Thus, for a given position on the bridge, several cantilever resonances can be measured with the same effective tip–sample contact stiffness. The microbridge sample was attached to the sample transducer with epoxy.

The effective tip–sample stiffness $k_{\text{eff}}(x_b)$ for a given contact position x_b can be described by a series combination of the contact stiffness k_H on thick, supported Si and the bending stiffness $k_b(x_b)$ of the microbridge at the contact location, i.e., $1/k_{\text{eff}}(x_b) = 1/k_H + 1/k_b(x_b)$. The stiffness $k_b(x_b)$ associated with bending of the microbridge is modeled as a clamped–clamped Euler–Bernoulli beam:

$$k_b(x_b) = \frac{3E_b I_b L_b^3}{(x_b)^3 (L_b - x_b)^3}, \quad (1)$$

where E_b , I_b , and L_b are Young’s modulus, bending moment of inertia, and length of the bridge, respectively. The stiffness k_H associated with the Si–Si tip–sample contact interface is modeled with Hertzian contact mechanics [22]. The system schematic in figure 1(b) shows the relation between the various stiffness components. The value of k_{eff} associated with an applied load of $\sim 100 \text{ nN}$ versus bridge position is shown in figure 1(c). k_{eff} values were determined experimentally from the average results of force–displacement [2] and CR-AFM experiments near the center of the bridge ($k_{\text{eff}} < 200 \text{ N m}^{-1}$), and from only CR-AFM experiments near the edge of the bridge ($k_{\text{eff}} > 200 \text{ N m}^{-1}$). For this calculation, the applied CR-AFM model included a tip–offset parameter and normal surface spring. k_{eff} has also been predicted

theoretically with equation (1) and the series spring equation. The theoretical value of k_H was chosen such that theory and experiment match at the edge of the bridge, and the theoretical value of $E_b I_b / L_b^3$ was chosen such that theory and experiment match at the center of the bridge. The gap between the Si bridge and the underlying substrate was approximately $1 \mu\text{m}$. This implies that the maximum static force that can be applied without contacting the bridge to the underlying substrate is about $3 \mu\text{N}$. Care was taken during the experiments to keep the maximum applied force well below this limit. It can be seen from equation (1) and an appropriate value for $E_b I_b / L_b^3$ that the value of k_b varies as a function of position x_b from an infinite value at the edge of the bridge to a value much less than k_H in the center of the bridge. k_{eff} is dominated by the softer of k_H or k_b if $k_b \ll k_H$ or $k_H \ll k_b$. k_H is known to be constant for a given applied load and contact geometry. Therefore, it can be inferred that $k_H = (1000 \pm 200) \text{ N m}^{-1}$ and $k_b = (5 \pm 2) \text{ N m}^{-1}$ when $x_b = L_b/2$ from data at the edge of the bridge and center of the bridge, respectively. It is often experimentally and theoretically convenient to use the dimensionless ratio $\alpha_{\text{eff}} = k_{\text{eff}}/k_c$, which is the normalized effective contact stiffness, to describe the sample-cantilever system. This allows for a more direct comparison of results obtained with different cantilevers.

Cantilever vibrational shapes were measured with the following procedure. The cantilever was brought into contact at a specified position on the microbridge and held at a constant normal force ($\sim 100 \text{ nN}$ for the stiffer cantilever A and $\sim 10 \text{ nN}$ for the more compliant cantilever B). The system was allowed to wait for 5 min to come into thermal, mechanical, and electrical equilibrium. After equilibrium was achieved, the feedback on the cantilever deflection was turned off, which locked out the motion of the Z-piezo and allowed

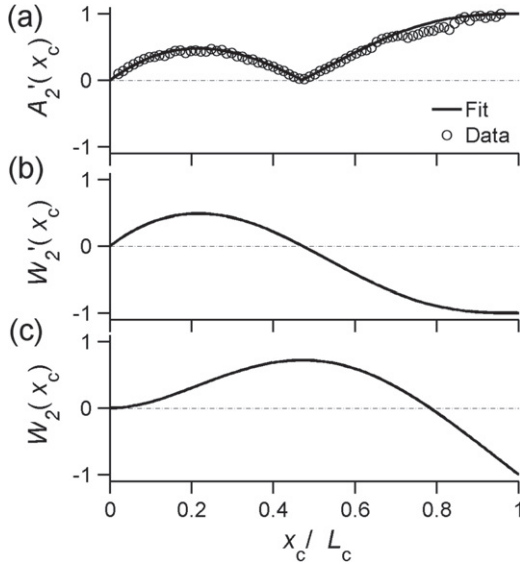


Figure 2. (a) Measured (circles) photodiode slope amplitude $A'_n(x_c)$ and corresponding absolute value of the best fit (line) from the Euler–Bernoulli model with arbitrary boundary conditions (equation (2) in text). (b) Cantilever slope shape $W'_n(x_c)$ obtained by reflecting $A'_n(x_c)$ about the antinode positions. (c) Cantilever eigenmode $W_n(x_c)$ determined from integration of $W'_n(x_c)$. Example is for the second resonance frequency of a freely vibrating cantilever.

repositioning of the laser spot without affecting the applied force. The laser was positioned close to the cantilever tip (i.e., at $x_c = L_c$). Then, a sinusoidal excitation voltage was applied to the sample transducer over a range of frequencies from 20 kHz to 4 MHz in 830 Hz increments. The cantilever vibrational shape was measured by recording the amplitude and phase of the photodiode response at each frequency for 80 equally spaced positions of the laser on the cantilever. The response in both the vertical and horizontal photodiode channels was recorded to distinguish flexural and torsional motions. The cantilever was then moved to a new position on the microbridge and the measurement repeated. Measurements were made at 60 equally spaced positions on the microbridge. A measurement of cantilever vibrational shape at a single bridge position took about 15 min. The vibrational shape measurement was also performed on the free cantilever (i.e., tip out of contact).

The optical detection system of the AFM measures cantilever slope rather than absolute displacement. Therefore, the raw experimental results correspond to the amplitude of the cantilever slope as a function of laser spot position, excitation frequency, and effective tip–sample stiffness. This raw result will be referred to as the cantilever ‘amplitude slope shape’ $A'(x_c)$, a typical example of which is shown in figure 2(a). To perform data analysis, it is necessary to convert the experimentally measured amplitude slope shapes into operating deflection shapes (ODSs). An ODS is the actual shape in which the cantilever vibrates at a specific excitation frequency. For the system studied here, the ODSs are identical to the cantilever eigenmodes $W_n(x_c)$, the solution to the Euler–Bernoulli beam equations, at the cantilever resonance frequencies. The conversion from $A'(x_c)$ to ODS is

accomplished by first reflecting the amplitude slope shape about its antinode positions to obtain the measured cantilever slope versus position. This will be referred to as the cantilever slope shape $W'_n(x_c)$; a typical example is shown in figure 2(b). $A'(x_c)$ is the absolute value of $W'_n(x_c)$. The slope shape $W'_n(x_c)$ is then fit to the following model:

$$W'_n(x_c) = C_1 \left[\cos(\beta_n x_c) - \cosh(\beta_n x_c) \right] - C_2 \left[\sin(\beta_n x_c) + \sinh(\beta_n x_c) \right], \quad (2)$$

where C_1 and C_2 are fitting parameters, and $\beta_n = 1.875 \sqrt{f_n/f_{1,free}}$ is the cantilever wavenumber. This model is derived from Euler–Bernoulli beam theory and holds for a cantilever beam regardless of the boundary conditions at the tip. The fitted model is then integrated to recover the cantilever eigenmode. A typical eigenmode recovered from this process is shown in figure 2(c).

A final experimental quantity that was computed is the slope amplitude integral I . I is the integral of the slope amplitude signal along the length of the cantilever: $I = \int_0^L A'(x) dx$. Use of I to locate resonance frequencies ensures that resonance peaks are not missed because of zero photodiode signal when the laser spot position is at a cantilever antinode. Use of I also increases the contrast of the resonance peaks relative to the background noise.

3. Results and discussion

Figure 3 shows the dependence of I on excitation frequency and normalized effective stiffness $\alpha_{eff} = k_{eff}/k_c$ for both cantilevers. This image is an experimental reconstruction of the CR-AFM ‘S-curves’, which depict the relationship between frequency and stiffness and were known previously only from theory [16]. By measuring two different cantilevers, we have covered a wide range of α_{eff} . Results are shown for the normalized frequencies $f/f_{1,free}$, so that the images for different cantilevers can be compared directly. The bright regions in the slope amplitude integral maps indicate the locations of the resonance frequencies of the surface-coupled cantilever. The flexural vibration modes show up primarily in the vertical (V) photodiode channel, while the lateral or torsional vibration modes show up primarily in the horizontal (H) photodiode channel. However, imperfections in alignment between the sample, excitation source, laser, cantilever, and photodiode mean that the flexural modes are also visible in the H channel, and the lateral or torsional modes are slightly visible in the vertical channel. It can be seen that the flexural resonant frequencies are much more sensitive to changes in contact stiffness than the resonance frequencies of the torsional or lateral modes. Furthermore, the flexural resonant frequencies vary nonlinearly from approximately the value for a clamped-free cantilever for low contact stiffness to near the value of a clamped-pinned cantilever for high contact stiffness. The measured resonance frequency values at three k_{eff} values for each cantilever are shown in table 1.

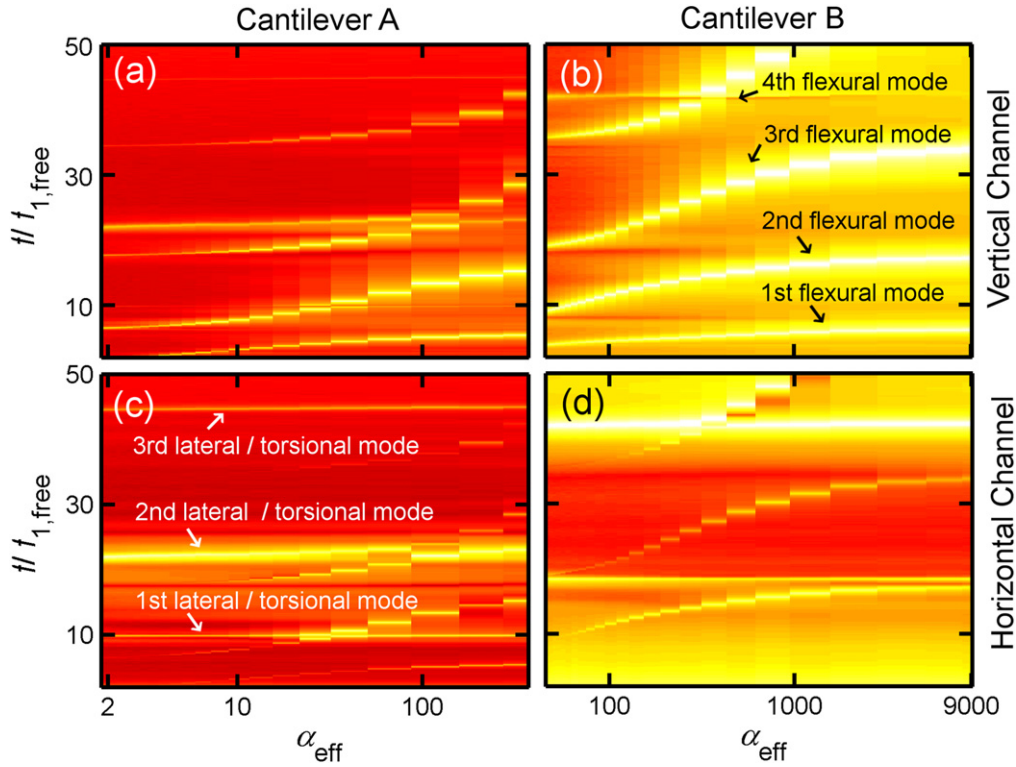


Figure 3. Images of the cantilever slope integral I as a function of normalized excitation frequency $f/f_{1,\text{free}}$ and normalized effective contact stiffness α_{eff} . The images in (a) and (c) were obtained on cantilever A for the vertical (V) and horizontal (H) photodiode signals, respectively, while (b) and (d) are the corresponding images for cantilever B. In the color scale, dark red represents the minimum and bright yellow the maximum. The color scale has units of volts and ranges logarithmically between 0.001 and 10. Some of the individual modes of vibration are labeled in the plots.

Table 1. Measured flexural resonance frequencies. Both the freely vibrating (free vibration) and in-contact frequencies (on supported silicon, $x_b \leq 0$, and at the bridge center, $x_b = L_b/2$) are listed. The range over which the flexural frequencies vary should be bounded by the theoretical predictions made with Euler–Bernoulli beam theory for a clamped-free beam [$\cos(\beta_n L_c) \cosh(\beta_n L_c) + 1 = 0$] and those for a clamped–clamped beam [$\cos(\beta_n L_c) \cosh(\beta_n L_c) - 1 = 0$], where $\beta_n = 1.875 \sqrt{f_n/f_{1,\text{free}}}$. The lowest two lateral and torsional resonance frequencies are located at ~ 731 kHz and ~ 3866 kHz for cantilever A and ~ 252 kHz and ~ 618 kHz for cantilever B. The lateral and torsional resonance frequencies do not change significantly with k_{eff} .

Cantilever	x_b	k_{eff} (N m ⁻¹)	f_1 (kHz)	f_2 (kHz)	f_3 (kHz)	f_4 (kHz)
A	Free vibration	0	75.9 ± 0.1	475.8 ± 0.1	1332 ± 1	2604 ± 1
	$L_b/2$	5 ± 2	132 ± 2	496 ± 1	1342 ± 1	2614 ± 1
	≤ 0	1000 ± 200	410 ± 9	1176 ± 24	2287 ± 93	3491 ± 276
B	Free vibration	0	12.6 ± 0.1	79.9 ± 0.1	224.3 ± 0.1	439.6 ± 0.1
	$L_b/2$	5 ± 2	48.6 ± 0.4	114 ± 1	240 ± 1	449 ± 1
	≤ 0	1000 ± 200	76.6 ± 0.3	216 ± 1	425 ± 2	709 ± 4

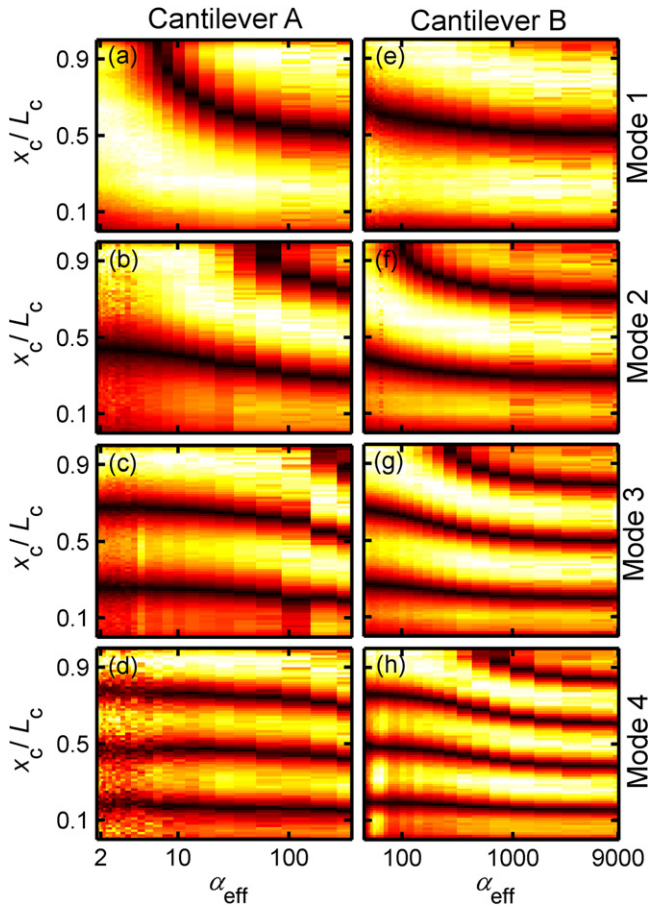


Figure 4. Cantilever amplitude slope shape $A'_n(x_c)$ as a function of normalized effective contact stiffness α_{eff} for both cantilevers A and B and modes 1 through 4. Each column in the figures has been normalized to vary between zero (black) and one (white), and represents $A'_n(x_c)$ at a given contact stiffness. The dark curves show the motion of the antinode positions.

For certain values of α_{eff} , the flexural and lateral or torsional modes have nearly the same resonant frequency. Here, the vibrational response of the AFM cantilever has repeated (closely spaced) eigenvalues [23, 24]. This behavior is often evidenced experimentally by a double peak in the contact resonance spectrum from the vertical photodiode channel. When analyzing spectra for a single point, this effect can make identification of the desired modes more difficult and can complicate CR-AFM imaging experiments [11–13, 25]. Thus, it is important to choose the cantilever for CR-AFM experiments such that the flexural and lateral or torsional resonance frequencies will not be near each other for a sample of interest and chosen cantilever eigenmode.

The CR eigenmodes $W_n(x_c)$ are usually determined from theoretical models such as Euler–Bernoulli beam theory. With our measurement procedure, we have directly measured changes in cantilever eigenmodes as a function of α_{eff} . Figure 4 shows normalized amplitude slope shapes at the first four resonant frequencies $A'_n(x_c)$ of the vertical photodiode channel as a function of α_{eff} and location on cantilever x_c/L_c . Because $A'_n(x_c)$ are extracted on resonance, (a) both frequency and stiffness change simultaneously along the x -axis

and (b) there is a simple relationship between $A'_n(x_c)$ and $W_n(x)$ as described in figure 2. Each column in figure 4 represents the cantilever amplitude slope shape at a given α_{eff} . Each row shows how the slope amplitude at resonance varies with α_{eff} for a given cantilever position x_c . Examination of figure 4 clearly shows that $A'_n(x_c)$ varies as a function of tip–sample stiffness. The shape changes nonlinearly from approximately that of a clamped-free cantilever at low effective stiffness to approximately that of a clamped-pinned cantilever at high effective stiffness. Over some stiffness ranges, the change in $A'_n(x_c)$ is very small, such as for $\alpha_{\text{eff}} > 1000$ for mode 1 of the softer cantilever B. Conversely, some stiffness regimes exhibit rapid change in $A'_n(x_c)$, such as α_{eff} from ~ 10 to ~ 100 for mode 1 of the stiffer cantilever A. The dark regions in figure 4 represent the cantilever’s antinodes of vibration. These antinodes are the maxima in cantilever displacement and hence have zero-valued cantilever slope. The figures illustrate the importance of choosing a laser spot position that avoids antinode locations when performing CR-AFM experiments.

From inspection of figures 3 and 4, it is apparent that both resonant frequency and amplitude slope shape are sensitive to changes in α_{eff} . Furthermore, both frequency and slope shape change monotonically with stiffness, suggesting that either quantity could be used to extract nanomechanical properties. However, it is difficult to quantitatively compare the relative sensitivity to stiffness without further processing of the data. For data reduction purposes, it is convenient to reduce the amplitude slope shape at a given value of α_{eff} to a single quantity. Options for this include the antinode positions, the ratio C_2/C_1 of the curve fitting constants in equation (2), the cantilever strain energy $\int_0^L W_n''(x_c) dx$, or the inner product of the contact mode with the free mode. Here we will use the inner product P between the measured surface-coupled eigenmode and the measured free eigenmode:

$$P_n = \int_0^L W_{n,\text{free}} W_{n,\text{cont}} dx \quad [26, 27].$$

Figures 5(a)–(h) show our measured results for the inner product P_n and resonance frequency f_n versus α_{eff} . The eigenmodes are mass normalized, that is $1 = \int_0^L W_n^2 dx$. For comparison, we also plot the values of P_n and f_n predicted by Euler–Bernoulli beam theory with a clamped boundary condition on one side and a spring boundary condition on the other [16]. The Euler–Bernoulli model agrees well (within $\sim 10\%$) with the experimental data for values of the normalized stiffness $\alpha_{\text{eff}} < 100$. The relatively poor agreement at higher α_{eff} is attributed to the lack of additional model parameters such as a lateral spring or relative tip position [16, 28]. From the figure, it is clear that the inner product provides a monotonic function of stiffness related to slope shape. Thus, P_n provides an alternate parameter for calculating tip–sample contact stiffness. P_n could either be used to independently calculate contact stiffness or could be used in conjunction with f_n as an additional observable parameter that is at the same frequency. A second observable parameter at the same frequency is especially important when tip–sample contact stiffness varies as a function of frequency and a model

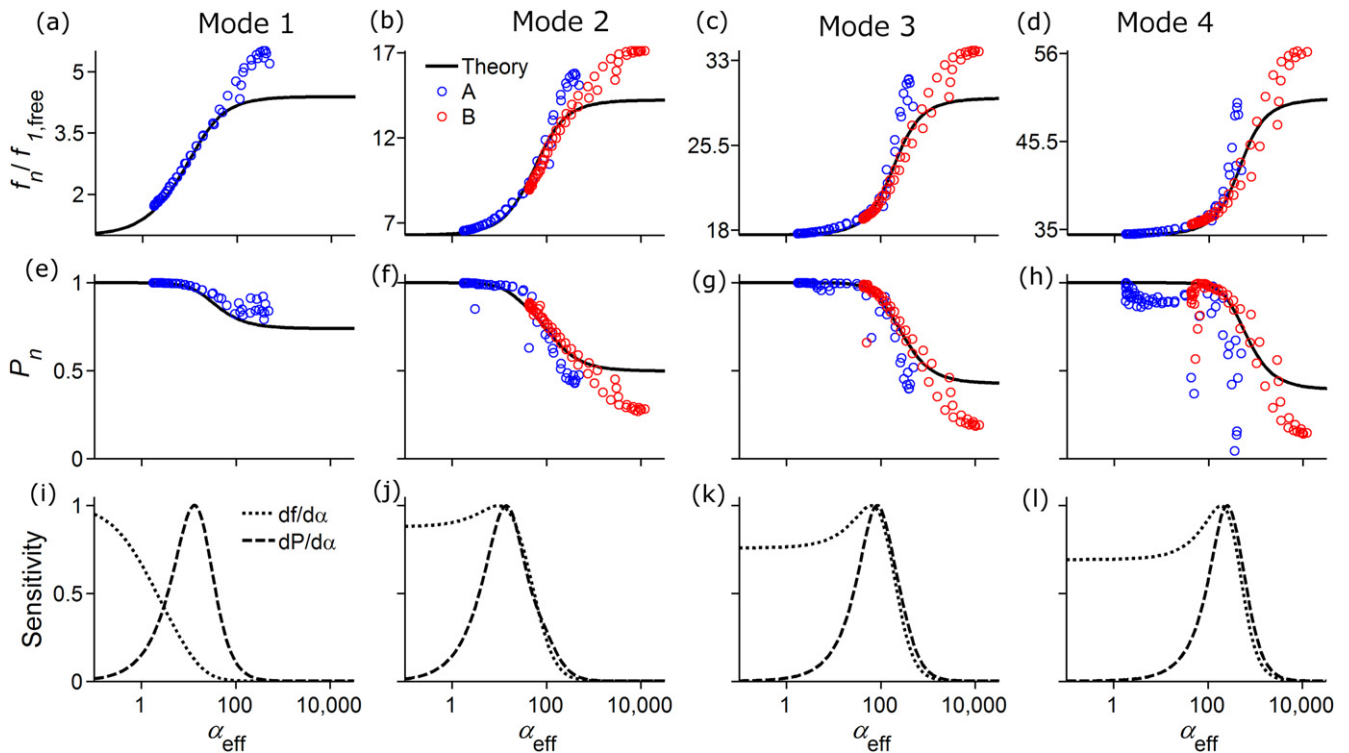


Figure 5. (a)–(d) Measured resonance frequencies f_n as a function of normalized effective contact stiffness α_{eff} for the first four modes with theory overlaid. (e)–(h) Measured inner product of free and surface-coupled mode shape P_n as a function of α_{eff} with theory overlaid. Blue circles: cantilever A, red circles: cantilever B, theory: black line; see text for details. (i)–(l) Comparison of normalized f_n sensitivity $df/d\alpha$ (dotted line) and P_n sensitivity $dP/d\alpha$ (dashed line) calculated from the analytical model. For the first mode the maximum in sensitivity of these two measurements occur at significantly different values α_{eff} .

with two unknown boundary conditions is needed. Common CR-AFM models with multiple unknown boundary conditions include models with both a normal stiffness and an offset tip position or models with both normal stiffness and a lateral spring. In traditional CR-AFM the second boundary condition would be found by taking measurements at a second resonance frequency. This traditional approach is not applicable if the material properties are frequency dependent.

From the theoretical model we can generate curves that are easily differentiated and thus allow for a discussion of sensitivity. The sensitivity of contact resonance frequency $df_n/d\alpha_{\text{eff}}$ and inner product $dP_n/d\alpha_{\text{eff}}$ to changes in stiffness are not equivalent. Our ability to accurately measure frequency is also much different from our ability to measure cantilever slope shape. Thus, absolute sensitivity values are not directly comparable. Instead, we limit discussion to noting the values of α_{eff} at which the maxima in sensitivity occur. Figures 5(i)–(h) show the sensitivity functions $dP_n/d\alpha_{\text{eff}}$ and $df_n/d\alpha_{\text{eff}}$ for modes $n = 1$ to $n = 4$. Each sensitivity curve has been scaled from 0 (minimum) to 1 (maximum) to facilitate comparison. For modes 2 through 4, the peak in $dP_n/d\alpha_{\text{eff}}$ occurs at values of α_{eff} that are $\sim 40\%$ greater than those for $df_n/d\alpha_{\text{eff}}$. The value of α_{eff} of maximum sensitivity increases for both $dP_n/d\alpha_{\text{eff}}$ and $df_n/d\alpha_{\text{eff}}$ as mode number n increases. The frequency sensitivity $df_n/d\alpha_{\text{eff}}$ is high for low values of α_{eff} and then decreases with increasing α_{eff} (that is, as the system approaches the clamped-pinned condition). In

contrast, $dP_n/d\alpha_{\text{eff}}$ is large only for a narrow range of α_{eff} . The most dramatic difference between $df_n/d\alpha_{\text{eff}}$ and $dP_n/d\alpha_{\text{eff}}$ occurs for mode 1. There, the maximum in $dP_1/d\alpha_{\text{eff}}$ occurs at $\alpha_{\text{eff}} \sim 14$, a stiffness where $df/d\alpha$ is only about 10% of its maximum value. This has practical implications for CR-AFM: measurement of the slope shape could expand the range of measurement sensitivity beyond that currently attainable with frequency data alone, particularly for mode $n = 1$.

The shape of the cantilever vibration also has practical applications for CR-AFM experiments. The dark regions in figure 4 correspond to the location of the antinodes of vibration. Because the optical beam deflection system used in most commercial AFMs is a slope detector, it is necessary to avoid positioning the laser spot near one of these antinode locations in a CR-AFM experiment. This is a nontrivial task, because the shape of cantilever vibration changes as a function of tip-sample stiffness. The applied beam model will not perfectly predict the cantilever eigenmodes because of inaccuracies in the model and uncertainties in the contact stiffness. Because of these imperfections, a theoretical prediction of slope shape will not be sufficient for determining optimal laser spot positions in certain CR-AFM experiments. For instance, the antinodes of the higher-order eigenmodes are spaced more closely together, so that smaller changes in laser spot position can have larger changes in observed amplitude. Another example is attempting to track multiple eigenmodes

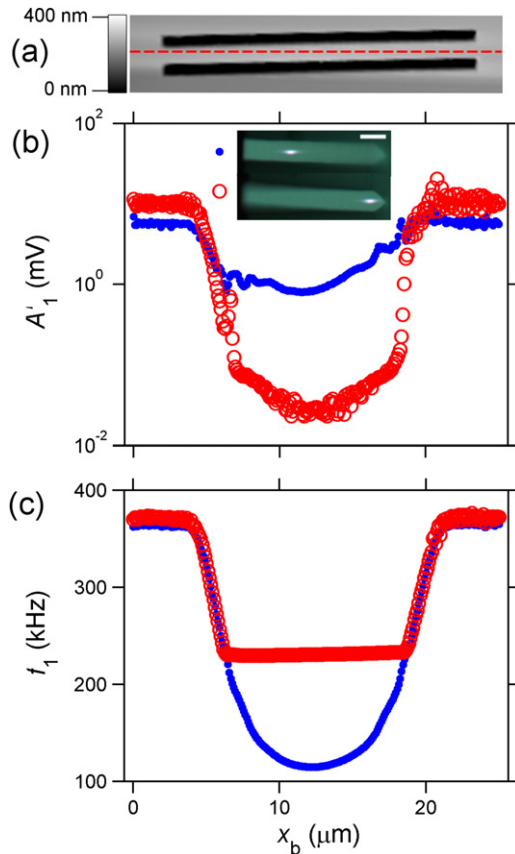


Figure 6. CR-AFM frequency tracking experiment using the first eigenmode of cantilever A. (a) AFM topography image of microbridge. Dashed line indicates the scan line for the frequency tracking experiment. (b) DART amplitude A_1' versus bridge position x_b for two laser spot positions, one near the base of the cantilever (blue dots) and one near the tip of the cantilever (red circles). Legend insets are optical microscope images showing the exact laser spot positions. The scale bar in the inset is $30\ \mu\text{m}$. (c) DART frequency f_1 tracking versus scan position for two laser spot positions. Frequency tracking capability of the system is lost when the antinode passes through the laser spot position and amplitude drops below the operational limit. Frequency data obtained after losing tracking is deemed unreliable.

simultaneously [12, 14], in which case the antinodes for each eigenmode should be avoided. In these situations, the best approach to determine optimal laser spot positions maybe to make an experimental measurement of slope shape with the method described in this work.

Movement of the antinode position along the cantilever can inhibit the application of CR-AFM to materials with a high range of contact stiffness. This is especially important for CR-AFM imaging methods, which require sufficient vibration amplitude of the resonance at all locations across the sample. To demonstrate this effect, we performed CR-AFM frequency-tracking experiments on the microbridge sample for the first eigenmode of cantilever vibration with two different laser spot positions with the dual amplitude resonance tracking (DART) method [13]. The results are shown in figure 6. Typically in AFM experiments, the laser spot is positioned near the end of the cantilever to maximize

quasistatic force sensitivity. As shown by the red data points in figure 6, this laser position provides high vibration amplitude and good frequency tracking on the stiffer edges of the bridge. However, when traversing along the bridge, the amplitude steadily drops to the point that tracking fails, and no reliable frequency information is obtained near the center of the bridge. Such a result could be predicted from figure 4(a), which shows an antinode crossing the chosen laser position for this particular stiffness range. By instead positioning the laser much closer to the clamped end of the cantilever (blue data points), the maximum amplitude at the stiff edges of the bridge is reduced, but the minimum amplitude on the more compliant portion of the bridge is much greater. At all times, the amplitude is high enough for successful frequency tracking with the base laser position. We conclude that it is necessary to choose a laser spot position on the cantilever that does not cross an antinode position over the stiffness range exhibited by the sample. For the first mode of vibration and for samples with a very large stiffness range, this will necessitate a laser position close to the cantilever base. However, for other modes of vibrations and other samples, there may be laser positions closer to the tip that maximize force sensitivity and vibration amplitude, while still avoiding antinode crossing. By obtaining slope shapes at the high and low stiffness limits of a sample under investigation, the optimal laser positioning can be determined. Alternatively, the results of figure 4 can serve to estimate the optimal laser positioning when cantilevers with similar geometry to those used here are employed.

4. Conclusions

The vibrational shapes and resonance frequencies of AFM cantilevers in contact with a surface have been measured over a wide and continuously varying range of effective contact stiffness. This was accomplished with use of an *in situ* laser scanning technique and a silicon microbridge sample. Cantilever vibration shape measurements exhibit a monotonic relationship between eigenmode inner product and contact stiffness. This suggests a potential alternate pathway for the direct measurement of unique contact stiffness values with CR-AFM. Furthermore, if combined with the measurement of contact resonance frequency, the mode shape provides an additional observable quantity that can be used to refine parameters in more complex CR-AFM models (e.g., ones that include tip position or lateral stiffness). This additional observable could be especially useful in situations where tip-sample stiffness depends on frequency, and thus data from different eigenmodes cannot be assumed to have the same boundary conditions. Results of the frequency tracking experiments combined with cantilever vibration shape measurements also provide users with practical guidelines for selecting the optimal laser spot position in CR-AFM experiments. We have demonstrated that the common practice of locating the laser spot near the tip of the cantilever is not always optimal and that the laser spot position should instead be adjusted on an individual sample and cantilever basis.

Finally, benefitting from the varying stiffness of the microbridge sample, our results validate CR-AFM frequency versus stiffness *S*-curves that previously had only been predicted by theory. Overall, the experimental results provide a wealth of new information with which to validate, analyze, and guide CR-AFM measurements. This information could not be obtained from data taken at a single laser spot position or at a single value of contact stiffness.

Acknowledgments

We are grateful to Jeffrey Hutter (University of Western Ontario, Canada) for providing the microbridge sample and Roger Proksch (Asylum Research / Oxford Instruments) for providing the original slope-shape measurement software. We also thank Robert Moon (Georgia Institute of Technology) for valuable discussions. Finally, we would like to acknowledge NSF grant number CMMI-0826356 for enabling the collaboration between NIST and Purdue.

References

- [1] Binnig G and Quate C 1986 Atomic force microscope *Phys. Rev. Lett.* **56** 930–3
- [2] Butt H-J, Cappella B and Kappl M 2005 Force measurements with the atomic force microscope: technique, interpretation and applications *Surf. Sci. Rep.* **59** 1–152
- [3] García R and Pérez R 2002 Dynamic atomic force microscopy methods *Surf. Sci. Rep.* **47** 197–301
- [4] Rabe U and Arnold W 1994 Acoustic microscopy by atomic-force microscopy *Appl. Phys. Lett.* **64** 1493–5
- [5] Yamanaka K, Ogiso H and Kolosov O 1994 Ultrasonic force microscopy for nanometer resolution subsurface imaging *Appl. Phys. Lett.* **64** 178–80
- [6] Rabe U, Janser K and Arnold W 1996 Vibrations of free and surface-coupled atomic force microscope cantilevers: theory and experiment *Rev. Sci. Instrum.* **67** 3281–93
- [7] Rabe U, Kopycinska M, Hirsekorn S, Saldaña J M, Schneider G A and Arnold W 2002 High-resolution characterization of piezoelectric ceramics by ultrasonic scanning force microscopy techniques *J. Phys. D: Appl. Phys.* **35** 2621
- [8] Hurley D C 2009 Contact resonance force microscopy techniques for nanomechanical measurements *Applied Scanning Probe Methods* ed B Bhushan and H Fuchs vol 11 (Berlin: Springer) pp 97–138
- [9] Stan G, Ciobanu C V, Thayer T P, Wang G T, Creighton J R, Purushotham K P, Bendersky L A and Cook R F 2009 Elastic moduli of faceted aluminum nitride nanotubes measured by contact resonance atomic force microscopy *Nanotechnology* **20** 035706
- [10] Killgore J P, Kelly J Y, Stafford C M, Fasolka M J and Hurley D C 2011 Quantitative subsurface contact resonance force microscopy of model polymer nanocomposites *Nanotechnology* **22** 175706
- [11] Yamanaka K, Maruyama Y, Tsuji T and Nakamoto K 2001 Resonance frequency and Q factor mapping by ultrasonic atomic force microscopy *Appl. Phys. Lett.* **78** 1939–41
- [12] Kos A B, Killgore J P and Hurley D C 2014 SPRITE: a modern approach to scanning probe contact resonance imaging *Meas. Sci. Technol.* **25** 025405
- [13] Gannepalli A, Yablon D G, Tsou A H and Proksch R 2011 Mapping nanoscale elasticity and dissipation using dual frequency contact resonance atomic force microscope *Nanotechnology* **22** 355705
- [14] Kopycinska-Müller M, Striegler A, Schlegel R, Kuzeyeva N, Koehler B and Wolter K-J 2012 Dual resonance excitation system for the contact mode of atomic force microscopy *Rev. Sci. Instrum.* **83** 043703
- [15] Melcher J, Hu S and Raman A 2007 Equivalent point-mass models of continuous atomic force microscope probes *Appl. Phys. Lett.* **91** 053101
- [16] Rabe U 2006 Atomic force acoustic microscopy *Applied Scanning Probe Methods II* ed B Bhushan and H Fuchs (Berlin: Springer) pp 37–90
- [17] Stan G and Solares S 2014 Frequency, amplitude, and phase measurements in contact resonance atomic force microscopies *Beilstein J. Nanotechnology* **5** 278–88
- [18] Zhou X, Fu J and Li F 2013 Contact resonance force microscopy for nanomechanical characterization: accuracy and sensitivity *J. Appl. Phys.* **114** 064301
- [19] Wagner R, Raman A and Proksch R 2013 Spatial spectrograms of vibrating atomic force microscopy cantilevers coupled to sample surfaces *Appl. Phys. Lett.* **103** 263102
- [20] Hutter J L and Bechhoefer J 1993 Calibration of atomic-force microscope tips *Rev. Sci. Instrum.* **64** 1868–73
- [21] Proksch R, Schäffer T E, Cleveland J P, Callahan R C and Viani M B 2004 Finite optical spot size and position corrections in thermal spring constant calibration *Nanotechnology* **15** 1344
- [22] Hertz H 1881 On the contact of elastic solids *Journal für die reine und Angew. Math.* **92** 156–71
- [23] Pierre C 1988 Mode localization and eigenvalue loci veering phenomena in disordered structures *J. Sound Vib.* **126** 485–502
- [24] Perkins N and Mote C 1986 Comments on curve veering in eigenvalue problems *J. Sound Vib.* **106** 451–63
- [25] Jesse S, Kalinin S V, Proksch R, Baddorf A P and Rodriguez B J 2007 The band excitation method in scanning probe microscopy for rapid mapping of energy dissipation on the nanoscale *Nanotechnology* **18** 435503
- [26] Huang J, Krougrill C and Bajaj A 2006 Modeling of automotive drum brakes for squeal and parameter sensitivity analysis *J. Sound Vib.* **289** 245263
- [27] Meirovitch L 1997 *Principles and Techniques of Vibrations* (Upper Saddle River, NJ: Prentice Hall)
- [28] Killgore J P and Hurley D C 2012 Low force AFM nanomechanics with higher-eigenmode contact resonance spectroscopy *Nanotechnology* **23** 055702